Future Changes in the Vertical Structure of Severe Convective Storm Environments over the U.S. Central Great Plains

ISAAC DAVIS,[a] FUNING LI,[b] AND DANIEL R. CHAVAS[b]

[a] *National Center for Atmospheric Research, Boulder, Colorado*
[b] *Department of Earth, Atmospheric, and Planetary Sciences, Purdue University, West Lafayette, Indiana*

(Manuscript received 21 March 2023, in final form 8 June 2024, accepted 24 June 2024)

ABSTRACT: The effect of warming on severe convective storm potential is commonly explained in terms of changes in vertically integrated ("bulk") environmental parameters, such as CAPE and 0–6-km shear. However, such events are known to depend on the details of the vertical structure of the thermodynamic and kinematic environment that can change independently of these bulk parameters. This work examines how warming may affect the complete vertical structure of these environments for fixed ranges of values of high CAPE and bulk shear, using data over the central Great Plains from two high-performing climate models (CNRM and MPI). To first order, projected changes in the vertical sounding structure are consistent between the two models: the environment warms approximately uniformly with height at constant relative humidity, and the shear profile remains relatively constant. The boundary layer becomes slightly drier (−2% to 6% relative humidity) while the free troposphere becomes slightly moister (+1% to 3%), with a slight increase in moist static energy deficit aloft with stronger magnitude in CNRM. CNRM indicates enhanced low-level shear and storm-relative helicity associated with stronger hodograph curvature in the lowest 2 km, whereas MPI shows near-zero change. Both models strongly underestimate shear below 1 km compared to ERA5, indicating large uncertainty in projecting subtle changes in the low-level flow structure in climate models. The evaluation of the net effect of these modest thermodynamic and kinematic changes on severe convective storm outcomes cannot be ascertained here but could be explored in simulation experiments.

SIGNIFICANCE STATEMENT: Severe thunderstorms and tornadoes cause substantial damage and loss of life each year, which raise concerns about how they may change as the world warms. We typically use a small number of common atmospheric parameters to understand how these localized events may change with climate change. However, climate change may alter the weather patterns that produce these events in ways not captured by these parameters. This work examines how climate change may alter the complete vertical structure of temperature, moisture, and wind and discusses the potential implications of these changes for future severe thunderstorms and tornadoes.

KEYWORDS: Severe storms; Storm environments; Thunderstorms; Tornadoes; Climate change; Climate models

1. Introduction

Severe convective storms (SCSs) produce large hail, strong convective wind gusts, and tornadoes, all of which pose a significant threat to life and property annually (Ashley 2007; Strader and Ashley 2015). It is thus of great interest to understand how SCS activity and its associated risks may change in the future as the climate warms. Future changes in risk are difficult to assess because severe thunderstorms are too small in scale to be resolved in modern climate models. Nonetheless, recent research using downscaling simulations that can resolve thunderstorm systems has found that proxies for SCS activity show broad increases in frequency and severity in the future over the United States as the climate warms (Ashley et al. 2023; Trapp et al. 2019; Hoogewind et al. 2017; Gensini and Mote 2015), with potential shifts in their spatial distribution and seasonal cycle.

Understanding these future changes in SCS activity is rooted in our understanding of how SCS outcomes are linked to the larger-scale thermodynamic environment within which these storms are generated (Ashley et al. 2023). Environments favorable for SCS activity ("SCS environments") are typically defined by the combination of a thermodynamic ingredient, given by convective available potential energy (CAPE), and a kinematic environmental ingredient, given by a 0–6-km bulk wind difference (S06; "bulk shear"). Tornado-favorable environments are often defined using a third environmental parameter, storm-relative helicity, that is often calculated within the lowest 1 km (Coffer et al. 2019, 2020). These parameters have been widely used to explain the historical spatiotemporal pattern of severe thunderstorms and tornadoes, particularly over the United States (Gensini and Brooks 2018; Taszarek et al. 2021; Coffer et al. 2020; Li et al. 2020; Hoogewind et al. 2017) but also globally (Brooks et al. 2003; Allen et al. 2011; Taszarek et al. 2020b, 2021; Chen et al. 2020). Note that these parameters represent necessary but not sufficient conditions for severe convective storms and tornadoes, as a triggering mechanism for convective initiation is also required, although this step is relatively poorly understood and, hence, not easily incorporated into environmental analyses (e.g., Ashley et al. 2023). In future climate projections, the increase in SCS activity over North America is explained principally by large projected increases in CAPE (Ashley et al. 2023; Tippett et al. 2015; Gensini 2021; Lepore et al. 2021; Seeley and Romps 2015; Diffenbaugh et al. 2013; Hoogewind et al. 2017), consistent with a theoretical

---

Corresponding author: Daniel R. Chavas, dchavas@purdue.edu

DOI: 10.1175/JCLI-D-23-0141.1

model that predicts a rapid increase in the continental diurnal maximum CAPE with warming (Agard and Emanuel 2017). Finally, tropospheric relative humidity is expected to remain relatively constant with warming based on observations and climate models (Douville et al. 2022), although this outcome has yet to be evaluated specifically in the context of SCS environments.

However, each of these environmental parameters is "bulk," i.e., vertically integrated measures of buoyancy or shear. Substantial research has shown that there are pathways to change SCS outcomes, including storm mode and intensity, that are independent of these bulk measures. This includes dependencies on the vertical distribution of buoyancy and shear (McCaul and Weisman 2001), low-level shear profile (Guarriello et al. 2018; Peters et al. 2023b), low-level thermal and moisture structure (McCaul and Cohen 2002; Brown and Nowotarski 2019), and hodograph curvature (Nixon and Allen 2022). Additionally, SCS outcome is sensitive to free-tropospheric relative humidity (Chavas and Dawson 2021; Lasher-Trapp et al. 2021; Jo and Lasher-Trapp 2022), due in part to its strong effects on entrainment dilution that reduces parcel buoyancy and CAPE (Peters et al. 2020a); however, CAPE itself is nearly insensitive to this quantity.

Thermodynamic and kinematic profiles are complex, which makes it difficult to define and interpret variations in their vertical structure. Recently, Chavas and Dawson (2021) have developed a simple model for the SCS environmental thermodynamic and kinematic sounding structure comprised of a boundary layer model and a free-tropospheric model. The model is consistent with how SCS environments are generated downstream of the Rocky Mountains (Carlson and Ludlam 1968; Doswell 2001; Agard and Emanuel 2017; Li et al. 2021). This sounding framework offers a foundation for defining the vertical structure of an SCS environment based on a relatively small number of parameters. Hence, the model may also provide a useful framework for defining key changes in the vertical structure in the future.

How the complete vertical structure of SCS environments, rather than simply bulk parameters, may change in a future climate has received relatively little attention to date. To fill this knowledge gap, we seek to answer the following research questions:

1) How do the vertical thermodynamic and kinematic structure of severe convective storm environments change in high-performing CMIP6 climate model projections over the central Great Plains?
2) Are the changes consistent between two high-performing climate models?

To answer these questions, we investigate how the vertical thermodynamic profiles (temperature, relative humidity, and moist static energy deficit) and kinematic profiles (wind shear and storm-relative helicity) in severe storm environments may change with future warming. We focus here on the central Great Plains, which is within the primary severe thunderstorm and tornado hotspot over North America, to minimize geographic and seasonal variability. There is evidence of a robust increase in tornadoes over the Southeast United States in recent decades (Gensini and Brooks 2018), although the nature and dynamics of SCS environments are known to differ in this region. As a result, mixing the two regions is not advisable, but future work may seek to expand this analysis to the Southeast United States. For our analysis, we take advantage of recent work that identified a small number of climate models that best reproduce the historical SCS environment climatology over North America (Chavas and Li 2022). We further use a simple model for the SCS environmental sounding from Chavas and Dawson (2021) as a guiding framework to define key parameters that capture the basic vertical thermodynamic and kinematic structure, although our results are not specific to that model in order to keep our findings general.

We detail our methodology in section 2. We present our results for future changes in the structure of SCS environments and discuss key outcomes in section 3. Finally, we summarize conclusions and avenues for future work in section 4.

2. Methodology

This work uses reanalysis and climate model data to examine future thermodynamic and kinematic changes in the vertical structure independent of changes in bulk SCS environmental parameters (CAPE and S06). To do so, we focus our analysis on a limited geographic region, to minimize regional variability in the climatology (Taszarek et al. 2020a), and within a fixed range of values of CAPE and S06, to minimize the effects of future changes in CAPE and S06 itself. We use soundings from March through September in a region over eastern Kansas and Nebraska within the central Great Plains bounded by 100°–95°W and 38°–43°N (Fig. 1a), which is the same subdomain used in Li et al. (2020), to focus on the primary severe convective storm season. We retain soundings with CAPE between 3000 and 6000 J kg^{-1} and S06 between 15 and 35 m s^{-1} to capture the principal regime of CAPE–S06 values associated with significant SCS activity in the historical record (Brooks et al. 2003; Li et al. 2020). Note that we choose a range of fixed absolute values of CAPE for simplicity to ensure that the actual CAPE values are similar, rather than a percentile range that would account for differences in the overall distribution. We further impose an upper bound on the magnitude of convective inhibition (CIN) of < 125 J kg^{-1} following Lepore et al. 2021 to avoid environments unlikely to allow convective initiation, although results are similar without this criterion; its inclusion eliminates relatively few soundings as shown below. For both the thermodynamic and kinematic vertical structure, we first compare ERA5 data to climate model historical experiments to examine similarities and biases of the models. We then analyze the changes between the future and historical period for each climate model.

For climate model analysis, we select two specific CMIP6 climate models (Eyring et al. 2016): MPI-ESM1-2-HR (MPI) and CNRM-ESM2-1 (CNRM). These two models were identified by Chavas and Li (2022) as the two highest performing models in the CMIP6 archive for reproducing the historical SCS environment climatology over North America. Chavas and Li (2022) demonstrated that climate models exhibit a very wide range of variability in the climatological representation

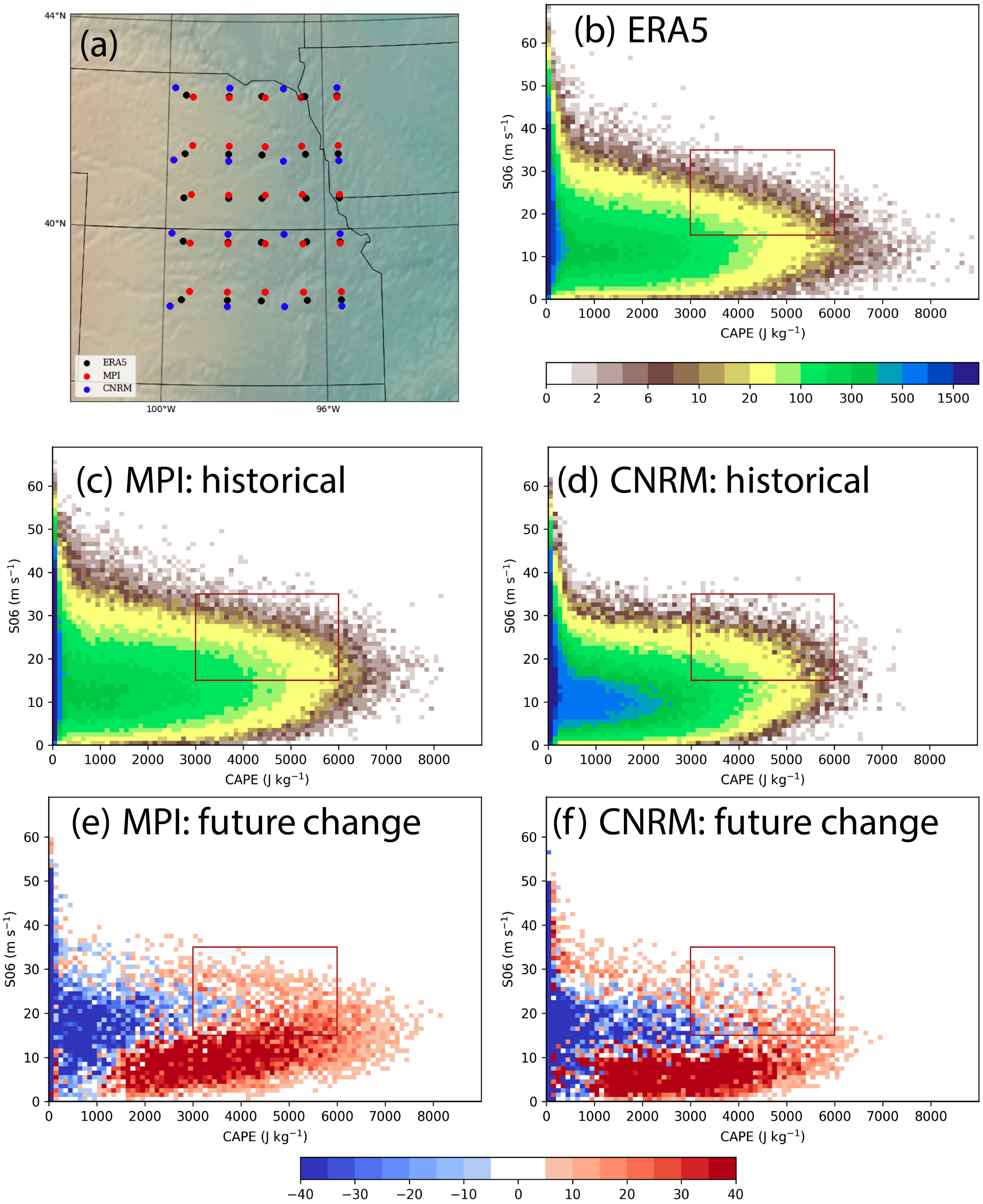

FIG. 1. (a) Map of gridpoint distributions within our region of interest from the ERA5 historical dataset and from the MPI and CNRM climate model datasets. (b) Joint histogram of CAPE and bulk shear (S06) from the ERA5 dataset for March–September for the period 1980–2014, with box denoting the fixed ranges of CAPE and S06 examined in this study. (c),(d) As in (b), but for MPI and CNRM, respectively. (e),(f) As in (c),(d), but for the difference between the future ssp370 (2065–99) and historical periods for each model. CNRM values have been multiplied by the factor 25/16 to account for its smaller number of grid points for an apples-to-apples comparison with ERA5 and MPI.

of severe convective storm environments (spatiotemporal pattern and amplitude) relative to historical data, and thus, it is important to first select models that can credibly reproduce the historical record. Although both models perform comparably well in reproducing the overall SCS environment climatology over North America, they still may differ in their representation of such environments specifically over our central Great Plains region of interest, as will be noted below. This outcome can be useful to check whether the models yield consistent responses in the vertical structure despite differing mean-state biases, which suggests greater robustness; this is a common approach when working with climate models for which the mean state (e.g., global-mean temperature) can vary across models, but the structure of their responses to forcing (atmospheric "fingerprint," e.g., spatial structure of warming due to increased greenhouse gas concentrations) may be quite similar (Santer et al. 2013; Zhang et al. 2023). We use the radiative forcing ssp370 experiment for each model as our future simulation, which is considered as a more plausible high-end forcing scenario than ssp585 (Pielke et al. 2022). The results for ssp585 are qualitatively similar (not shown). The historical period used is 1980–2014, and the future period is 2065–99.

We compare the climate model output against the ERA5 reanalysis model-level data for the identical period to match the climate model historical period (Hersbach et al. 2020). Model-level data ensure the use of the highest vertical resolution data available, although the results are similar when using ERA5 pressure-level data (not shown). ERA5 is sampled at 0000, 0600, 1200, and 1800 UTC to match the same 6-h output available from both climate models. ERA5 is the highest resolution of existing global long-term reanalysis datasets and performs well in reproducing the climatological spatiotemporal distribution of SCS environments found in radiosonde observations (Li et al. 2020). The vertical resolution of ERA5 (137 levels) and the two climate models (95 levels for MPI and 91 levels for CNRM) differ, so for direct comparison between ERA5 and the climate model data, we linearly interpolate the model data in the vertical to match ERA5. The horizontal resolution for ERA5 is $\Delta x = \sim 31$ km, $\Delta x = \sim 100$ km for MPI, and $\Delta x = \sim 140$ km for CNRM. We downsample ERA5 to every fourth grid point to more closely match the spacing of the models; the grids for each within our domain of interest are displayed in Fig. 1a. ERA5 and MPI both contain 25 grid points with the resolution of MPI being slightly finer, while CNRM contains 16 grid points. In contrast to the vertical grid, we do not interpolate data horizontally to the same grid to avoid mixing soundings at adjacent grid points that represent very different environments, such as in the vicinity of a cold front, which is not uncommon for SCS environments.

For a given sounding, we define the tropopause as the lowest altitude where the lapse rate drops below 2 K km^{-1} (WMO/OMM/BMO 1992; Chavas and Li 2022) and define the top of the boundary layer as the height of maximum relative humidity following Chavas and Dawson (2021). We calculate CAPE, given by

$$\mathrm{CAPE} = \int_{z_{\mathrm{LFC}}}^{z_{\mathrm{EL}}} g \frac{T_{vp} - T_{ve}}{T_{ve}} dz, \tag{1}$$

where $g = 9.81$ is the acceleration due to gravity; z is the altitude with subscripts "LFC" and "EL" denoting the level of free convection and equilibrium level, respectively; and T_v is the virtual temperature with subscripts "p" and "e" denoting parcel and environment, respectively. CAPE is calculated using the xcape codebase (Lepore et al. 2022) for the near-surface ($z = 2$ m) parcel as in Chavas and Li (2022). Bulk wind shear within a layer between bottom altitude z_b and top altitude z_t is given by the magnitude of the vector wind difference across the layer,

$$S(z_b)(z_t) = |\mathbf{V}_{z_t} - \mathbf{V}_{z_b}|. \tag{2}$$

For the standard 0–6-km shear layer (S06), $z_b = 10$ m and $z_t = 6000$ m. Finally, storm-relative helicity (SRH) is given by

$$\mathrm{SRH}_{0-z_t} = \int_{10\mathrm{m}}^{z_t} (\mathbf{V} - \mathbf{C}) \cdot (\nabla \times \mathbf{V}) dz, \tag{3}$$

where $\mathbf{V}$ is the wind vector at a given level, $\mathbf{C}$ is the storm-motion vector, and z_t is defined in the same manner as with shear. In our results below, we analyze wind shear variations between the surface and 6 km and SRH integrated over layers between the surface and 3 km. All parameters involving wind (hodographs, wind shear, and SRH) are calculated using the hodograph, storm-relative helicity, and Bunkers storm motion functions from MetPy v1.1 (May et al. 2022).

The climatological joint histogram of CAPE and S06 for ERA5 is shown in Fig. 1b and for the historical periods in MPI and CNRM, respectively, in Figs. 1c and 1d. Our fixed ranges of high CAPE and S06 values are highlighted by the red box, which is the same in each subplot. Because CNRM contains fewer grid points than ERA5 and MPI, we rescale the histogram data for CNRM by the factor 25/16 to account for its smaller number of grid points for an apples-to-apples comparison across all datasets. Both models do very well in reproducing the structure of the climatological joint distribution of CAPE and S06. Relative frequencies peak at moderate S06 (10–15 m s^{-1}) and small values of CAPE, and the largest CAPE values are associated with these moderate values of S06, consistent with past work (Li et al. 2020; Taszarek et al. 2020b). Within our phase space subset of interest (the box), CNRM captures both the structure and magnitude very well, while MPI captures the structure, but its magnitude has a clear high bias. Future changes in this joint distribution relative to historical within each model are shown in Figs. 1e and 1f. In the future, in both models, the phase space distribution shifts principally rightwards, associated with an increase in the frequency of relatively high CAPE (>3000 J kg^{-1}) but minimal change in S06 (Figs. 1e,f), again consistent with past research (Lepore et al. 2021). Within our phase space subset of interest, this shift represents an increase in the absolute frequency of such environments (predominantly red colors). Overall, then, both models perform reasonably well in reproducing the climatology of SCS environments, with MPI better capturing the overall magnitude of the joint histogram, consistent with the findings of Chavas and Li (2022), but CNRM better capturing the magnitude specifically within our specific CAPE–S06 subset.

The monthly and diurnal frequency distributions of our final sounding datasets are shown in Fig. 2. In ERA5, the seasonal cycle of SCS environments (Fig. 2a) closely follows the seasonal cycle of observed severe thunderstorm hazards and tornadoes for this region (Figs. 5 and 6 of Taszarek et al. 2020a), with a rapid increase from March through June, a peak in June/July, and then, a rapid decrease from July through October. CNRM does very well in reproducing the ERA5 seasonal cycle structure and amplitude, particularly for April through July, with a moderate high bias in August and September. Meanwhile, MPI also captures the structure but exhibits a strong high bias in magnitude that is consistent throughout the season. In the future, both models exhibit a

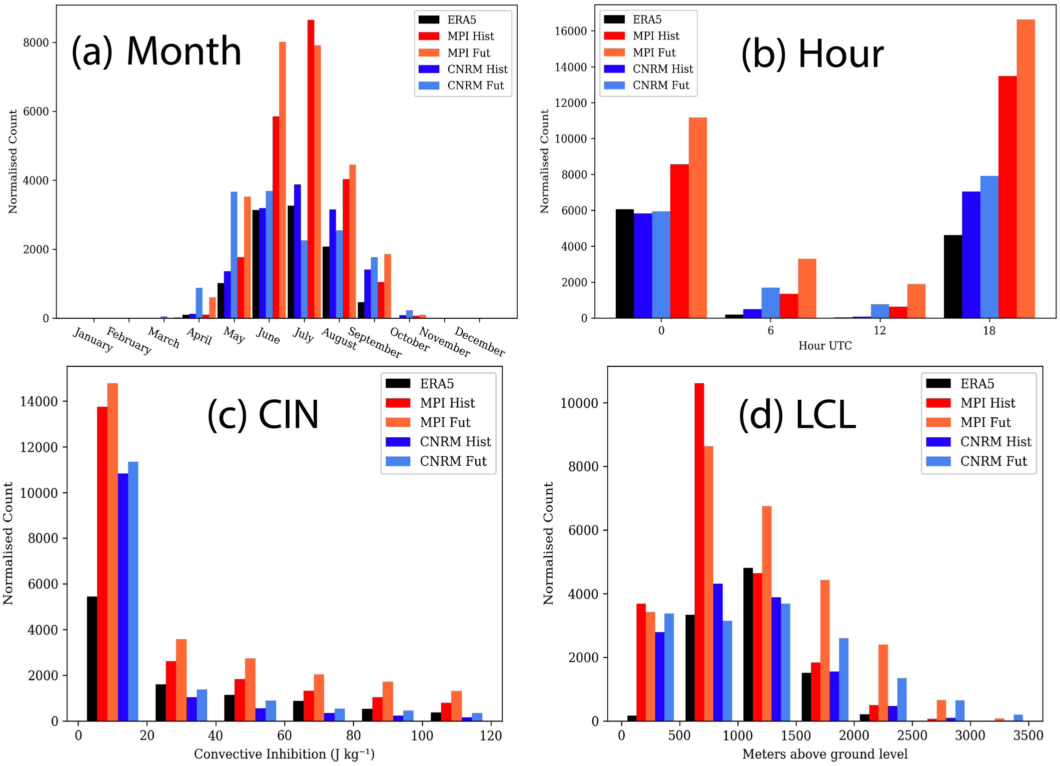

FIG. 2. (a) Monthly frequency of final subset for ERA5, MPI historical and ssp370 future, and CNRM historical and ssp370 future. (b) Diurnal frequency of final subset (0000/0600/1200/1800 UTC). (c) Frequency distribution of CIN within final subset in 20 J kg^{-1} bins starting from 0. (d) Frequency distribution of LCL within final subset in 500-m bins starting from 0. CNRM values have been multiplied by the factor 25/16 to account for its smaller number of grid points for an apples-to-apples comparison with ERA5 and MPI.

shift in the seasonal cycle toward earlier months (May/June) as has been found in recent work (Ashley et al. 2023).

The diurnal cycle (Fig. 2b) is skewed strongly toward afternoon/evening as expected, with the vast majority of soundings in ERA5 at 0000 UTC (~55%) and 1800 UTC (~45%) and very few events at 0600 and 1200 UTC. While 1800 UTC may seem early relative to the typical timing of convective storm occurrence in the late afternoon (Fig. 8 of Taszarek et al. 2020a), this difference likely reflects a lag between the gradual daytime generation of these soundings and the initiation of convection itself. CNRM captures the ERA5 diurnal cycle structure and amplitude well, although its distribution is shifted toward 1800 UTC, i.e., a bias toward too early in the day. MPI again captures the gross diurnal cycle structure with an overall strong high bias in magnitude, but notably, it exhibits a similar timing bias toward 1800 UTC as CNRM. This early timing bias may be associated with the known and early timing bias in inland precipitation itself that has been persistent in climate models possibly tied to deficiencies in convective parameterizations (Christopoulos and Schneider 2021). In the future, the distribution of soundings across the diurnal cycle remains relatively constant. We note that it is possible as this timing bias could result in biases in model projections of changes in SCS environments, although we are unable to evaluate this possibility here.

Finally, we examine the frequency distributions of CIN (Fig. 2c) and of lifted condensation level (LCL; Fig. 2d). CIN frequency peaks at relatively small values in ERA5 as well as in both climate models. There is a long tail of relatively low frequencies for higher CIN values up to our upper-bound threshold, and as a result, this criterion is already met for nearly all soundings that met our CAPE and S06 thresholds. MPI yields similar relative frequencies to ERA5, while CNRM is skewed more strongly toward smaller values. Both models reproduce the CIN distributions within SCS environments found in ERA5 relatively well. In the future, the relative frequency shifts toward slightly higher CIN, as the frequency of the lowest CIN bin increases by a significantly smaller percentage (+10%) than the higher bins (e.g., +25% for 60–80 J kg^{-1}). This increase in CIN with warming has been found in numerous past downscaling studies (e.g., Ashley et al. 2023).

As for the LCL, in ERA5, the frequency distribution peaks at 1000–1500 m though with relatively high frequency within 500–1000 m as well. Both models are biased toward slightly lower LCLs, with slightly higher frequencies at 500–1000 m in CNRM and a more pronounced low-LCL bias in MPI. Both climate models show a shift in their relative frequencies toward higher LCLs, suggesting a shift toward the drier boundary layer as will be found below.

Overall, the above examination of the spatial, seasonal, and diurnal variability lends credence that our sounding database is broadly representative of environments favorable for severe

TABLE 1. Key quantities calculated from the mean thermodynamic profiles from ERA5, MPI, and CNRM, including those relevant to the SCS sounding model of Chavas and Dawson (2021). Values are the mean with interquartile range (25th–75th percentiles) in parentheses. Range not included for boundary layer height as this quantity can be noisy for individual cases. The asterisk denotes that the future change is statistically significant at the 95% confidence level.

	ERA5	MPI-ESM1-2-HR		CNRM-ESM2-1	
		HIST	FUT	HIST	FUT
2–6-km lapse rate (K km^{-1})	7.2 (6.8, 7.6)	7.3 (6.9, 7.7)	7.1 (6.7, 7.5)*	7.2 (6.8, 7.6)	7.2 (6.7, 7.6)*
2–10-km lapse rate (K km^{-1})	7.3 (7.1, 7.6)	7.4 (7.2, 7.6)	7.3 (7.0, 7.5)*	7.5 (7.3, 7.7)	7.4 (7.1, 7.7)*
Tropopause temp (K)	207.8 (204.9, 210.4)	207.8 (204.9, 210.4)	213.5 (211.3, 215.9)*	208.6 (206.7, 210.6)	210.0 (207.5, 212.5)*
Tropopause height (km)	14.8 (14.7, 14.9)	13.9 (13.8, 14.0)	14.0 (13.9, 14.2)*	13.1 (12.9, 13.2)	13.2 (13.1, 13.4)*
0–1-km avg RH (%)	64.0 (56.2, 72.7)	71.8 (63.7, 80.5)	65.2 (53.6, 76.7)*	66.7 (54.2, 80.2)	64.5 (49.3, 80.4)*
1–2-km RH lapse rate (% km^{-1})	20.8 (3.4, 36.7)	19.0 (4.6, 32.3)	14.7 (1.3, 26.6)*	6.2 (−4.2, 16.2)	5.0 (−6.0, 15.5)*
2–6-km avg RH (%)	40.4 (29.7, 50.2)	47.0 (34.2, 58.2)	48.6 (36.4, 59.8)*	59.8 (49.1, 71.2)	61.2 (51.2, 72.4)*
2–10-km avg RH (%)	35.9 (26.1, 44.5)	46.1 (33.4, 57.9)	48.5 (36.6, 59.7)*	53.8 (42.8, 65.4)	56.2 (46.1, 67.2)*
BL Height (km)	0.7	0.4	0.7	0.8	1.1
BL MSE (kJ kg^{-1})	342.6 (339.4, 346.1)	345.3 (341.8, 349.1)	348.9 (345.4, 353.0)*	335.3 (332.4, 338.6)	340.4 (336.3, 344.8)*
BL DSE (kJ kg^{-1})	308.8 (306.8, 310.6)	307.6 (305.4, 309.6)	310.2 (307.2, 313.2)*	305.9 (303.5, 308.1)	308.6 (305.4, 311.5)*
2–6-km avg MSE deficit (kJ kg^{-1})	17.5 (14.8, 20.2)	16.6 (13.8, 19.4)	16.7 (13.7, 19.6)	14.6 (12.4, 16.5)	14.8 (12.3, 17.0)*
2–10-km avg MSE deficit (kJ kg^{-1})	15.6 (12.9, 18.1)	15.4 (12.8, 17.8)	15.6 (12.9, 18.2)*	13.3 (11.3, 15.0)	13.9 (11.7, 15.9)*

convective storms and that our two climate models perform reasonably well in reproducing these environments. For our region and the CAPE–S06 subset of interest, CNRM appears to be the slightly better model given its much smaller amplitude bias. As noted above, the contrasting mean-state amplitude biases provide useful context for our analysis, as responses of the vertical structure to forcing that are consistent between the two models suggest that they are less likely to be sensitive to biases in the climate model mean state.

3. Results

a. Changes in thermodynamic vertical structure

1) TEMPERATURE

We begin by examining changes in the thermodynamic vertical structure simulated by both models. For all of the analyses below, values of some key quantities, including those relevant to the framework of Chavas and Dawson (2021), are provided in Table 1 for additional reference.

Mean temperature profiles from both models for the historical climate are compared with ERA5 in Fig. 3a. MPI performs well in reproducing the vertical structure of temperature found in ERA5, with temperatures decreasing rapidly with height above the surface within a well-mixed boundary layer and then decreasing more slowly above the boundary layer before decreasing more rapidly again through the free troposphere. The model compares well with ERA5, with small biases of <1 K in magnitude through the depth of the troposphere. CNRM also reproduces the vertical structure of the temperature profile, though with a substantial overall cool bias of approximately 5 K throughout the troposphere; the bias is smaller (3.5 K) within the boundary layer. The result that MPI better captures mean-state temperature is consistent with Chavas and Li (2022). While these contrasts in gross temperature bias between models may seem surprising, it is common for climate models to have differing mean-state biases yet exhibit similar structural responses to forcing, as noted earlier.

Despite different magnitudes of mean bias, both models closely match the mean lapse rate within the free troposphere found in ERA5 of 7.2 K km^{-1} for 2–6 km and 7.3 K km^{-1} for 2–10 km, respectively (Table 1). Moreover, both models closely match the tropopause temperature of 208 K. Both models also capture the magnitude of variability in temperature, with a relatively small variability of <3 K magnitude in the interquartile range throughout the troposphere (Fig. 3a). The primary qualitative difference in the vertical thermal structure between the models is that MPI better captures the transition layer of reduced lapse rate separating the boundary layer and free troposphere found in ERA5.

Future changes in the simulated temperature profiles for each model are shown in Fig. 3b. Both models project future thermal structures that are qualitatively similar to their historic simulations but simply shifted nearly uniformly warmer through the depth of the troposphere by approximately 2 K. CNRM warms slightly more than MPI at all levels above

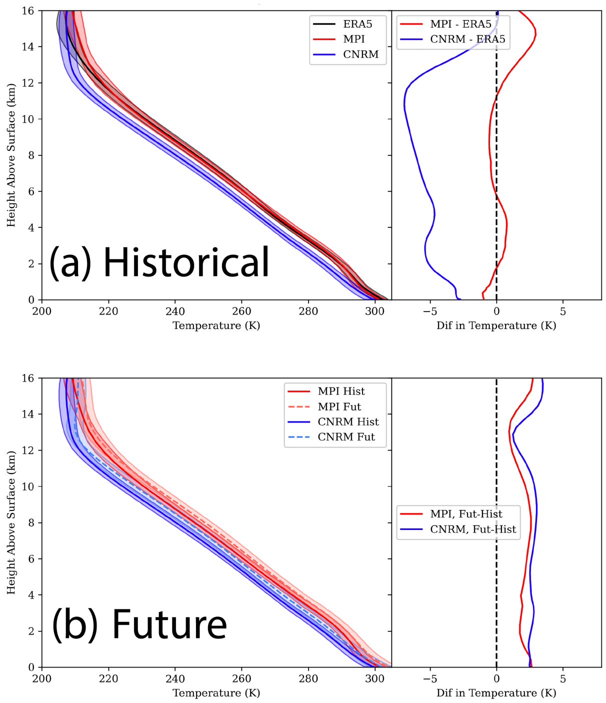

FIG. 3. (a) Mean vertical profiles of temperature from ERA5 and the historic runs of MPI and CNRM. The shaded area represents the interquartile range (25th–75th percentiles), and the difference plot shows the differences between the ERA5 and MPI, and ERA5 and CNRM. (b) As in (a), but for the historic and future runs of MPI and CNRM. The difference plot shows the differences between the future and historic simulations of each model.

1 km. In both models, the free-tropospheric lapse rates decrease very slightly (Table 1), by 0–0.2 K km^{-1} for both the 2–6-km and 2–10-km layers. The tropopause temperature warms by 1.4 K in CNRM and 5.7 K in MPI, while the tropopause height increases slightly. This is in contrast to the expectation of an upward expansion of the troposphere at fixed tropopause temperature (Singh and O'Gorman 2012; Seeley et al. 2019; Thompson et al. 2019). Moreover, the thermal structure sharpens around the tropopause including a sharper temperature increase above the tropopause, which may have impacts on the depth and strength of overshooting tops (O'Neill et al. 2021).

Overall, despite some significant differences in historical vertical thermal structure biases between the two models, their future climate responses are similar. This outcome gives greater confidence in the ability to use these models to quantify future changes in the thermal structure of SCS environments.

2) RELATIVE HUMIDITY

We next examine the vertical structure of relative humidity (RH) in Fig. 4. Note that we focus on relative humidity rather than absolute humidity since we are examining changes in the moisture structure across a range of temperatures and tropospheric relative humidity is expected to remain relatively constant with warming as noted in introduction. Mean RH profiles from both models for the historical climate are compared with ERA5 in Fig. 4a. MPI performs well in reproducing the gross vertical structure of RH found in ERA5, with RH increasing with height above the surface toward a local maximum near the top of the well-mixed boundary layer and then decreasing sharply up to approximately 2.5-km altitude before becoming relatively constant with height through the rest of the free troposphere. The model is moister than ERA5, with a moist RH bias of 8% within the lowest 1 km, near-zero bias through the 1–2-km transition layer, and a moist RH bias of 5%–15% within the free troposphere (7% for 2–6 km mean; 10% for 2–10-km mean). MPI does capture the mean 1–2-km RH lapse rate of 20% found in ERA5. CNRM also reproduces the vertical structure of the RH profile, though with a smaller boundary layer bias and larger moist bias through both the transition layer and lower free troposphere below 6 km, with a peak moist bias of 22% at 3-km altitude. This latter moist bias indicates a much slower decrease in the RH between the moist boundary layer and drier free troposphere (1–2-km RH lapse rate of 6%). This behavior is consistent with the weaker thermal transition layer (Fig. 3a), which suggests stronger shallow convective mixing through the top of the boundary layer and into the lower free troposphere in CNRM (e.g., Hu et al. 2022).

Note that there is a much larger range of variability in RH across soundings relative to temperature (cf. width of interquartile shading with Fig. 3a). These ranges of variability are also well captured by the models. This distinction is a clear indication of how free-tropospheric moisture can vary widely on short spatial and temporal scales, as its local structure depends on the transport by antecedent convection and the mesoscale and synoptic-scale flow, all of which may vary strongly in space and time. In contrast, free-tropospheric temperatures are much more strongly constrained by the larger-scale dynamics of the midlatitude atmosphere.

Despite their different mean bias structures, both models do capture the gross vertical structure of RH, with the primary contrast in the transition layer between the boundary layer and the free troposphere. Moreover, both models reproduce the magnitude of variability in the RH.

Future changes in the simulated RH profiles for each model are shown in Fig. 4b. Both models project weak future changes in the RH, with slightly higher RH through the middle and upper free troposphere and slightly lower RH in the boundary layer. In the free troposphere, RH in both models increases by approximately 1.5% for the 2–6-km mean and 2.3% for the 2–10-km mean (Table 1). A larger increase in the RH occurs near the top of the free troposphere. At low levels, MPI and CNRM RH decreases by 6.5% and 2.2%, respectively, for the 0–1-km mean. In the transition layer, the 1–2-km RH lapse rate decreases slightly in both models (−4.3% in MPI and −1.2% in CNRM). Overall, the future climate responses of both models are again quite similar despite significant differences in their historical biases.

3) MOIST STATIC ENERGY DEFICIT

Finally, we examine the vertical structure of the moist static energy (MSE) deficit profile due to its close link to entrainment. The MSE deficit is defined as the difference between

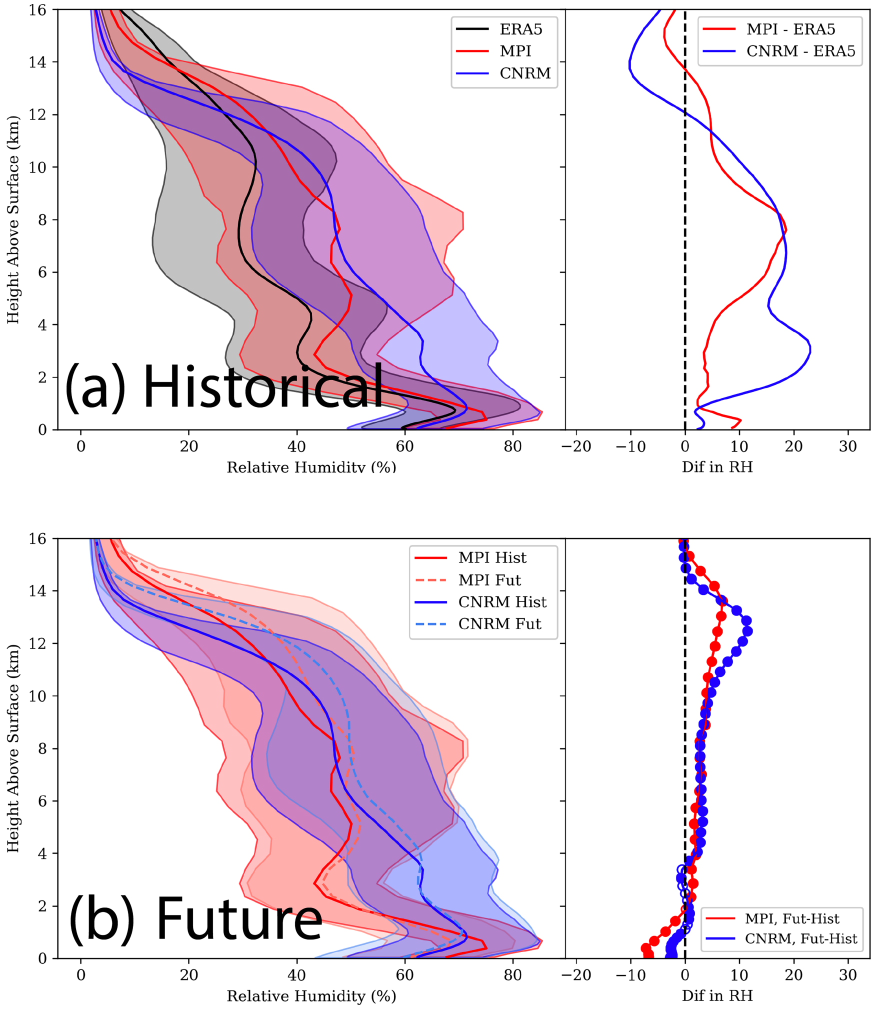

FIG. 4. (a) Mean vertical profiles of RH from ERA5 and the historic runs of MPI and CNRM. The shaded area represents the interquartile range (25th–75th percentiles), and the difference plot shows the differences between the ERA5 and MPI, and ERA5 and CNRM. (b) As in (a), but for the historic and future ssp370 runs of MPI and CNRM. The difference plot shows the differences between the future and historic simulations of each model. In (b), a filled circle indicates that the means are statistically significantly different at the 95% confidence level.

the MSE of the parcel at the lowest model level (LML) and the MSE of the environment at each level:

$$\mathrm{MSE}_{\mathrm{def}}(z) = \mathrm{MSE}(z_{\mathrm{LML}}) - \mathrm{MSE}(z). \tag{4}$$

The MSE is the sum of potential, sensible, and latent energies, i.e.,

$$\mathrm{MSE} = gz_p + C_pT + L_vq_v, \tag{5}$$

where C_p is the specific heat capacity of air, L_v is the specific latent heat of vaporization of water, $z_p = z + z_{p,\mathrm{sfc}}$ is the geopotential height with $z_{p,\mathrm{sfc}}$ being the geopotential height of the surface, and q_v is the water vapor mass fraction (specific humidity); we neglect the latent energy content of water ice as it is generally small. Its dry counterpart, dry static energy (DSE), neglects the latent energy term. The DSE and MSE are closely analogous to dry and equivalent potential temperature, respectively (Betts 1974; Chavas and Dawson 2021; Chavas and Peters 2023). The MSE deficit represents the energy difference between a parcel rising through a deep convective cloud and the surrounding near-cloud environment. To keep the calculation simple, the parcel MSE is assumed to be adiabatically conserved, thereby neglecting the MSE sink due to buoyancy (Peters et al. 2022). Entrainment is a process that mixes a parcel with the environmental air, and the energy a parcel loses per unit height is commonly parameterized in classical plume updraft models as proportional to the MSE deficit (e.g., Betts 1975; Zhang 2009). This process dilutes the buoyancy of rising air parcels and hence reduces the true CAPE realized by the parcel (Peters et al. 2023a). Thus, an increase in MSE deficit would imply an increase in entrainment in deep convective clouds, all else equal.

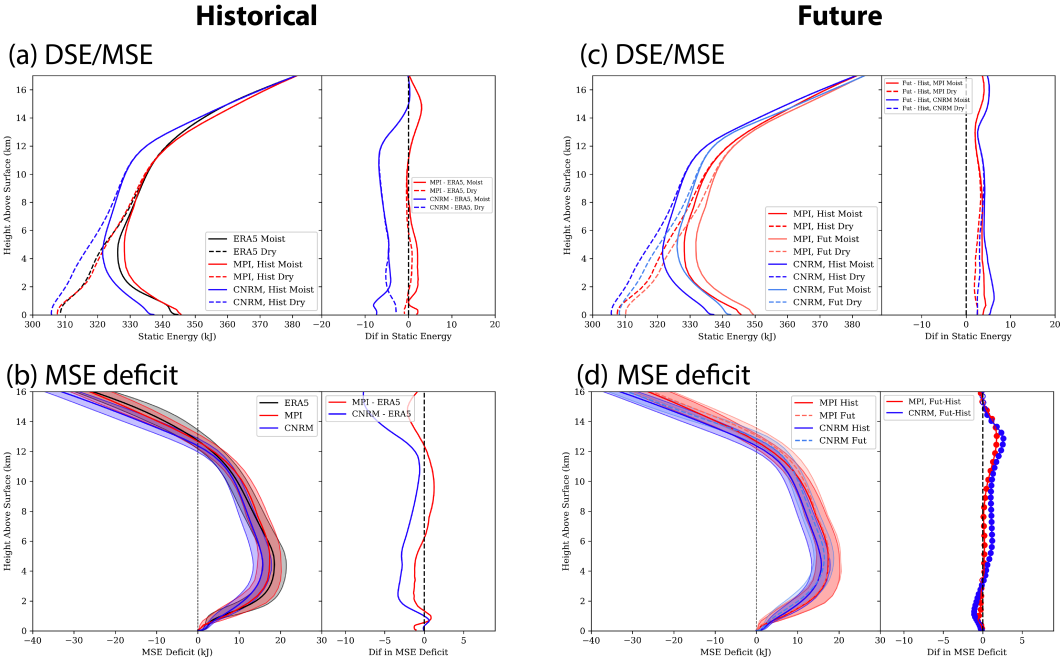

FIG. 5. (a) Mean vertical profiles of DSE and MSE from ERA5 and the historic runs of MPI and CNRM. The difference plot shows the differences between the ERA5 and MPI, and ERA5 and CNRM. (b) As in (a), but for MSE deficit, calculated for a parcel lifted from the LML assuming adiabatic conservation of MSE. The shaded area represents the interquartile range (25th–75th percentiles). (c),(d) As in (a),(b), but for the future ssp370 and historic simulations of both models. In (d), a filled circle indicates that the means are statistically significantly different at the 95% confidence level.

Since the MSE deficit profile is calculated from the MSE profile itself, we begin with vertical profiles of DSE and MSE for both models and ERA5 in Fig. 5a. Model biases in DSE profiles are unsurprisingly very similar to biases in temperature discussed previously (Fig. 3). Biases in MSE combine the energetic effects of biases from temperature and moisture. This yields an MSE bias structure that is very similar to the DSE in the free troposphere, where the latent energy content is much smaller than sensible energy, but more similar to the relative humidity bias within the boundary layer, where the latent energy content is much larger. MPI reproduces the full vertical profiles of MSE and DSE remarkably well, while CNRM also reproduces their structures but with a systematic low bias that is relatively constant with height.

Mean MSE deficit profiles from both models for the historical climate are compared with ERA5 in Fig. 5b. Both models perform well in reproducing the MSE deficit as compared to ERA5, with errors of <4 kJ kg^{-1} for CNRM and <2 kJ kg^{-1} for MPI throughout the troposphere. The largest errors are located near the boundary layer top and are likely associated with discrepancies in the boundary layer height. This is particularly true for MPI due to its bias in the boundary layer height (Table 1), whereas this bias is small in CNRM. Notably, the variability in the MSE deficit profiles is much smaller than for relative humidity (Fig. 4), suggesting that there may be strong covariability between the boundary layer and free-tropospheric MSE; this question is intriguing but lies beyond the scope of this work.

Future changes in the DSE and MSE profiles are shown in Fig. 5c. DSE increases relatively uniformly with height in line with changes in the temperature found above. MSE also increases relatively uniformly with height, though with slightly larger increases in the lowest 2 km particularly in CNRM. This outcome is not obvious from our previous analyses, but given that MSE is approximately conserved in deep convection, this suggests that to first order, convection (as parameterized in the models) acts to mix MSE vertically and hence homogenize its changes in a convectively active region.

Future changes in the MSE deficit profile are shown in Fig. 5d. MPI projects near-zero change in MSE deficit within the troposphere up to 10 km, while CNRM projects a small decrease of up to 1 kJ kg^{-1} beneath 4 km and a small increase of 1 kJ kg^{-1} between 4 and 10 km. The structure of change is similar between the two models, with the largest magnitude changes occurring near the tropopause. The modest increase in MSE deficit in the free troposphere is consistent with the finding that the MSE profile increases relatively uniformly with height as noted above, with a slight increase in the MSE within the boundary layer in CNRM.

Overall, the thermodynamic structure to first order warms relatively uniformly with height at approximately constant relative humidity. There is a slight drying of the boundary layer and slight moistening of the free troposphere, and there is a slight increase in the MSE deficit aloft. These projected changes are similar between our two model simulations despite differences in their representation of the historical climate. This outcome

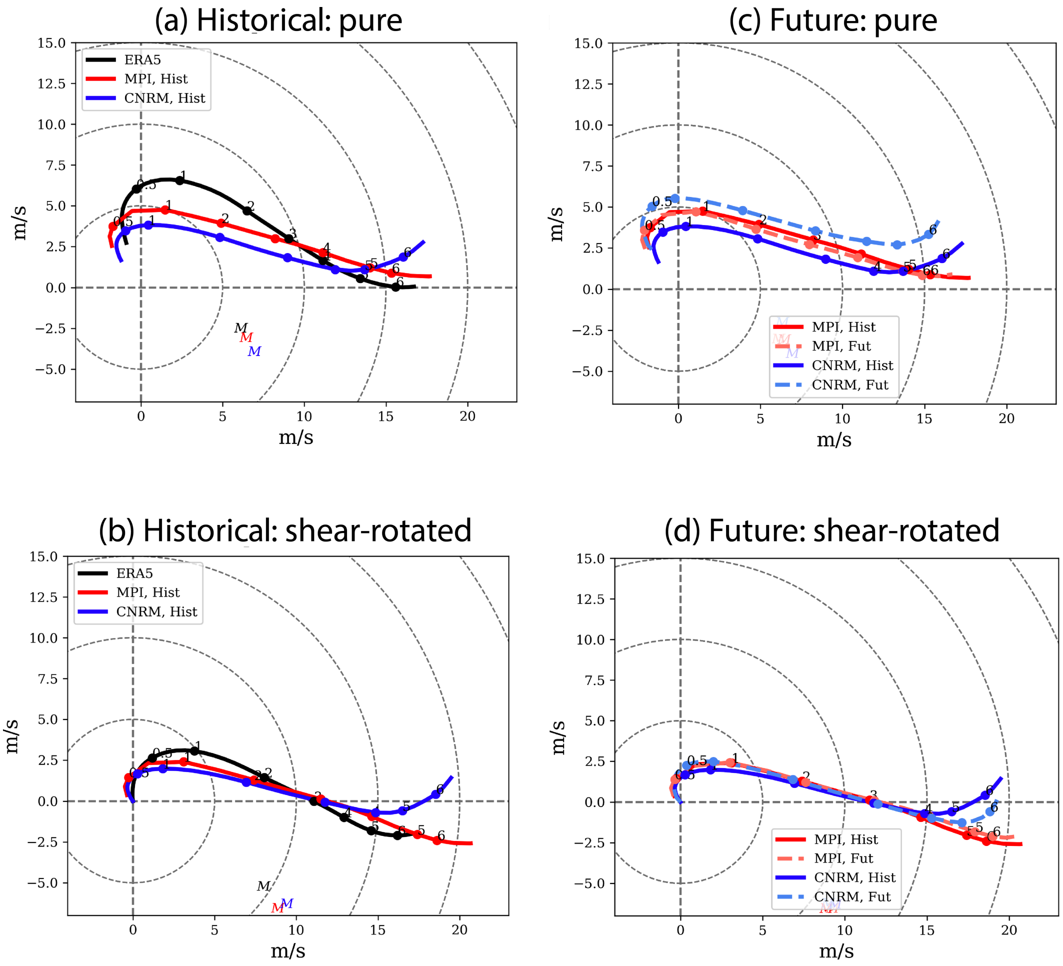

FIG. 6. (a) Composite hodographs for ERA5 and the historic runs of MPI and CNRM. Dots correspond in order to the altitudes (0.5, 1, 2, 3, 4, 5, and 6 km), and the Bunkers storm motion is shown, plotted as an "M." (b) As in (a), but for composite vector shear profiles, calculated by first subtracting the 10-m wind from each individual hodograph and then rotating the result such that the 0–3-km shear lies along the positive x axis (bottom row) following Nixon and Allen (2022). (c),(d) As in (a),(b), but for the future ssp370 and the historic runs of MPI and CNRM.

provides greater confidence in the robustness of the projected changes.

b. *Changes in kinematic structure*

We now examine the vertical structure of the lower-tropospheric winds associated with SCS environments. Figure 6 displays the composite hodographs (top row) as well as composite vector shear profiles calculated by first subtracting the 10-m wind from each individual hodograph and then rotating the result such that the 0–3-km shear lies along the positive x axis (bottom row) following Nixon and Allen (2022). The former provides insight into the true mean flow structure and its geographic orientation, while the latter represents a shear-relative composite that is more precise for examining the composite shear structure relevant to thunderstorm dynamics particularly within the 0–3-km layer. Because the qualitative flow structure is quite similar across hodographs, the results are not fundamentally different between the two approaches; we present both as they complement one another. Figure 7 then displays the vertical structure of vertical shear and storm-relative helicity calculated from the hodograph database (note: this analysis is calculated for each individual hodograph and so is independent of the composites). For all of the analyses below, values of some key quantities, including those relevant to the framework of Chavas and Dawson (2021), are provided in Table 2 for additional reference.

Mean hodographs from both models for the historical climate are compared with ERA5 in Fig. 6a, with the rotated vector shear profiles in Fig. 6b. MPI and CNRM are both quite similar to one another, and both reproduce the qualitative L-shaped vertical structure of the hodograph common in SCS environments (Guarriello et al. 2018; Coffer et al. 2020; Chavas and Dawson 2021) and also found in ERA5. This structure is characterized by a boundary layer of predominantly southerly shear in the lowest 0.5 km, with the southerly component of the flow increasing in magnitude with height.

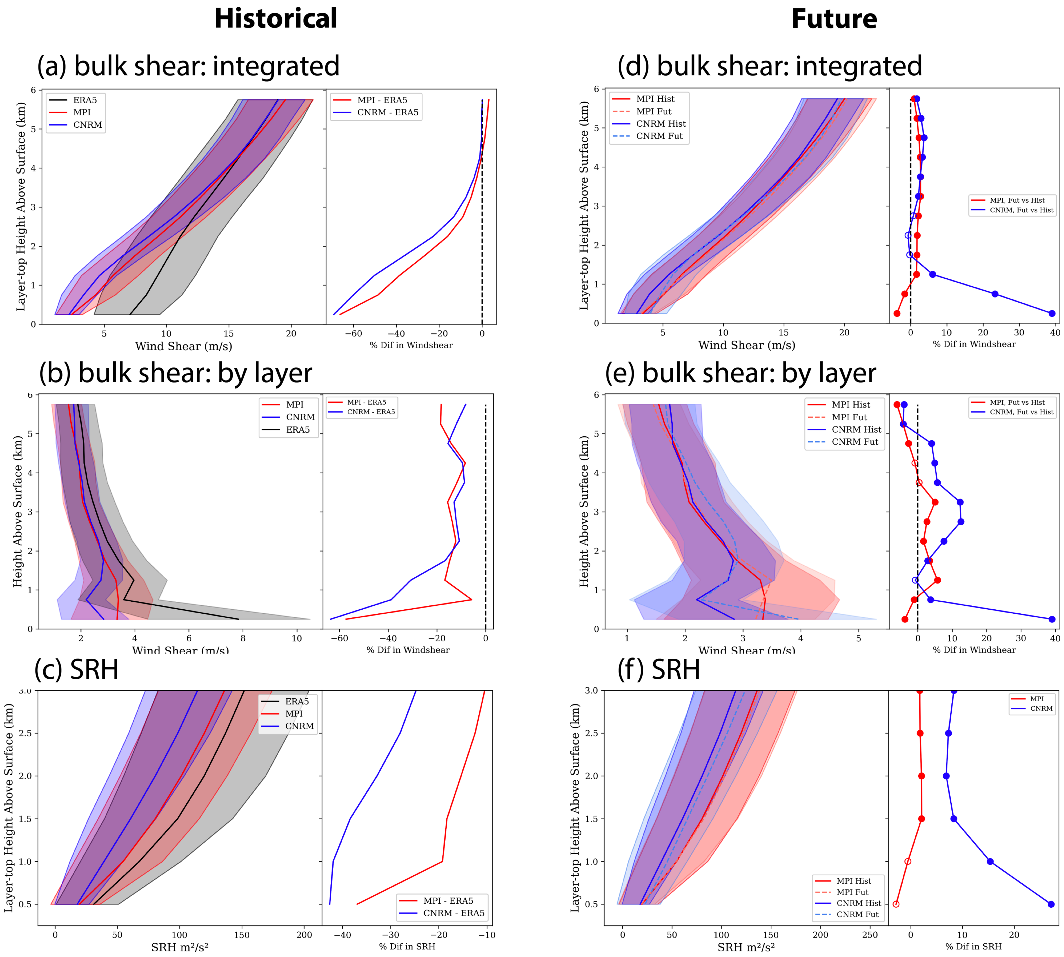

FIG. 7. (a) Bulk shear integrated from the surface up to layer-top altitudes up to 6 km, for ERA5 and the historic runs of MPI and CNRM. (b) As in (a), but for the vertical profile of bulk shear calculated layerwise every 500 m (plotted point is at layer center). (c) As in (a), but for SRH up to 3 km. (d)–(f) As in (a)–(c), but for the future ssp370 and the historic runs of MPI and CNRM. The solid line denotes the mean, and the shaded area represents the interquartile range (25th–75th percentiles); the difference plot shows the differences between the ssp370 future and historic simulations of both models. For the differences in (d)–(f), a filled circle indicates that the means are statistically significantly different at the 95% confidence level.

Overlying this boundary layer flow is a layer of predominantly westerly shear as the flow transitions from principally southerly to southwesterly to westerly moving upward to 6-km altitude. In ERA5, the shear in the lower free-troposphere has a northerly component that results in a sharper wind direction shift moving across the boundary layer top before becoming unidirectional similar to the models. Both simulations have a weaker southerly wind speed in the lowest 2 km, resulting in a hodograph that is shifted slightly to the south relative to ERA5. However, the Bunkers storm-motion vector of both models are similar to one another and are also shifted southeastward of the ERA5 vector by 1–2 m s^{-1}. Hence, the storm-relative flow does not change significantly, consistent with the similar hodograph translation at all heights. The surface flow vector is also very similar in both models. The lone notable difference between the two model hodographs is the shear between 0.5 and 2 km, where the wind vector changes more rapidly within the 0.5–1-km layer in MPI and within the 1–2-km layer in CNRM. The interpretation is similar for the composite rotated shear profiles (Fig. 6b): the shear structure is very similar between the two models below 4 km and is notably flatter than in ERA5. The differing low-level hodograph structure alters the shear distribution within the 0.5–2-km layer, which we discuss next.

Figure 7a shows bulk shear from the surface up to layer-top altitudes from 500-m to 6-km altitude, calculated from each individual hodograph in our dataset. Figure 7b displays the vertical profile of bulk shear (units: m s^{-1}) calculated layerwise within 500-m depth layers. The former directly visualizes the integrated bulk shear over any desired layer depth, while the latter visualizes the vertical distribution of shear biases (note though that integrated bulk shear biases need not equal the sum of the layerwise biases since shear is a vector difference). In each case, we show the differences relative to ERA5

TABLE 2. Key quantities calculated from the mean hodographs from ERA5, MPI, and CNRM, including those relevant to the SCS sounding model of Chavas and Dawson (2021). Values are the mean with interquartile range (25th–75th percentiles) in parentheses. "Hbl" refers to the boundary layer height. The asterisk denotes that the future change is statistically significant at the 95% confidence level.

	ERA5	MPI-ESM1-2-HR		CNRM-ESM2-1	
		HIST	FUT	HIST	FUT
Zonal surface U (m s^{-1})	−0.9 (−2.4, 0.5)	−1.5 (−3.2, 0.1)	−1.7 (−3.4, −0.0)*	−1.2 (−3.0, 0.6)	−1.6 (−3.3, 0.1)*
Meridional surface V (m s^{-1})	2.7 (0.6, 5.0)	2.1 (−1.4, 5.6)	2.0 (−1.3, 5.5)*	1.7 (−0.8, 4.0)	2.4 (−0.2, 5.0)*
Total shear 0–Hbl (m s^{-1})	8.4 (4.7, 11.2)	2.9 (1.3, 3.9)	4.0 (1.9, 5.3)*	3.4 (1.6, 4.5)	5.0 (2.3, 6.8)*
Zonal 0–Hbl U (m s^{-1})	1.6 (−1.6, 4.7)	−0.2 (−1.1, 0.6)	0.7 (−0.8, 2.0)*	1.1 (−0.1, 2.2)	2.1 (0.1, 3.5)*
Meridional 0–Hbl V (m s^{-1})	3.8 (−1.4, 8.8)	1.6 (−0.2, 3.1)	2.5 (0.2, 4.4)*	2.1 (0.2, 3.5)	3.1 (0.3, 5.4)*
Total shear Hbl–3 km (m s^{-1})	11.6 (8.6, 14.4)	12.6 (9.8, 15.0)	12.1 (9.3, 14.7)*	10.9 (8.3, 13.2)	9.9 (7.5, 12.2)*
Zonal Hbl–3 km U (m s^{-1})	8.5 (5.3, 11.7)	10.3 (7.4, 13.1)	9.3 (6.2, 12.3)*	8.9 (6.1, 11.5)	7.6 (5.0, 10.2)*
Meridional Hbl–3 km V (m s^{-1})	−3.6 (−8.3, 0.9)	−0.8 (−6.2, 4.1)	−1.8 (−7.3, 3.0)*	−1.9 (−6.0, 2.0)	−1.8 (−6.0, 2.2)*
Total shear 3–6 km (m s^{-1})	9.2 (6.4, 11.7)	9.4 (7.0, 11.6)	9.3 (6.8, 11.5)*	9.1 (6.6, 11.3)	9.4 (6.8, 11.6)*
Zonal 3–6 km U (m s^{-1})	6.2 (3.0, 9.3)	7.2 (4.6, 9.9)	6.9 (4.1, 9.5)*	7.2 (4.7, 9.7)	7.1 (4.5, 9.7)*
Meridional 3–6 km V (m s^{-1})	−2.9 (−6.8, 0.9)	−2.1 (−5.7, 1.3)	−1.8 (−5.7, 1.8)*	0.0 (−3.8, 3.4)	−0.4 (−4.4, 3.6)*

as percentages to compare the magnitude of the change across different layer depths. In ERA5, integrated bulk shear is small near the surface (7 m s^{-1} at 250 m) and then increases at a relatively constant rate with height, from 10 m s^{-1} at 2 km up to nearly 20 m s^{-1} at 6 km. This behavior is also evident in the layerwise bulk shear profile that decreases rapidly from 8 m s^{-1} in the lowest 500 m to 4 m s^{-1} between 1 and 2 km and then further decreases gradually toward 2 m s^{-1} above 4 km. Both models are similar to one another in reproducing this overall structure, consistent with their very similar hodographs, but both substantially underestimate low-level shear (>50% underestimation for 0–500-m shear). CNRM underestimations are slightly larger in the lowest 1.5 km relative to MPI owing to the different distribution of shear within 0.5–1.5 km described above. The models also consistently underestimate layerwise shear by 20% above 2 km, although these biases translate to relatively small biases (<5%) when integrated in a deeper-layer shear of 5–6 km (Fig. 7a). Hence, both models do very well in reproducing S06 yet exhibit large low biases in bulk shear for layers closer to the surface.

Similarly, Fig. 7c shows SRH up to layer-top altitudes from 0.5 to 3 km. In ERA5, SRH gradually increases with increasing layer-top altitude as expected given the two-layer structure of the hodograph. The results are again qualitatively similar for the two models. Both models have a moderate low bias in SRH relative to ERA5 at all levels, with MPI having consistently smaller biases than CNRM. The bias is the smallest for the 0–3-km layer (−10% and −30% for MPI and CNRM, respectively) and increases in magnitude moving toward shallower layers. Since SRH is equal to twice the vector area of the hodograph layer relative to the storm-motion vector, the low bias in SRH in the two models arises due to the weaker southerly component of the flow in the lowest 1 km of their hodographs relative to ERA5 in Fig. 6a (i.e., flatter shear profile in Fig. 6b). However, MPI exhibits slightly stronger curvature within this layer that is closer to that found in ERA5, and hence, the magnitude of its SRH biases is consistently smaller. This difference can also be interpreted as due to the low bias in shear in the lowest 1 km seen in Fig. 7b, as this low shear bias is effectively integrated upward with height to yield the low biases in SRH, an effect amplified for the shallowest layers.

Future changes in the simulated hodographs in each model are shown in Fig. 6c, with changes in the rotated vector shear profiles in Fig. 6d. The hodograph and storm-motion vector for MPI remain nearly constant, while for CNRM, they are to first-order simply translated north-northwestward. As a result, the shear-rotated hodographs are nearly constant for both models, with the exception of CNRM exhibiting slightly stronger curvature in the lowest 1 km due to slightly stronger southerly shear.

The change in integrated bulk shear is shown in Fig. 7d, and changes in the vertical distribution of bulk shear are shown in Fig. 7e, along with the percentage differences in future relative to historical for each. The percent change in integrated bulk shear is relatively small (<+2%) for all layer-top altitudes > 2 km and in both models, consistent with the minimal change in shear-relative hodographs found above. Recall that for our analysis, we restricted our range of S06 values to focus on future changes in the vertical structure for a given value of bulk environmental parameters, and hence, the 0–6-km wind shear is nearly constant in both models. In the lowest 1 km, MPI exhibits only a small decrease in shear integrated bulk shear, as again its shear-relative hodograph changes minimally. In contrast, in CNRM, integrated bulk shear increases within the lowest 1 km, with the largest increase of 40% for 0–500 m. This strong increase in near-surface shear in CNRM is associated with the stronger southerly near-surface shear in the hodograph noted above. These outcomes are also evident in the changes in layerwise bulk shear profiles, with the lone notable difference being that CNRM exhibits more substantial increases in shear within the 2–5-km layer associated with a subtle reduction in the curvature of the hodograph (Fig. 7a), although these layerwise directional shear changes have a relatively small impact when integrated over a deeper layer such as for S06. Overall, the wind shear changes over all layer depths are modest, except for an enhanced shear within the lowest 1 km in only one of the two models, indicating significant uncertainty in this outcome. Moreover, it is important to note that the model biases relative to ERA5 were also the largest in the lowest 1 km and were similar between the two models, which further reduces confidence in determining which model outcome might be considered more likely.

The change in SRH is shown in Fig. 7f, along with the percentage differences in future relative to historical. The qualitative structure of the changes in SRH mirrors the changes in integrated bulk shear discussed above (Fig. 7d). For MPI, SRH changes are very small ($<5\%$) given that the hodograph remains nearly constant. Meanwhile, CNRM shows an increase in SRH over all layer depths. Changes are smaller for the layer-top altitudes of 1.5–3 km ($+5\%$–10%), whereas for 1 km and below, SRH increases more strongly, including $+25\%$ for the 0–500-m layer. This increase in SRH is associated with the increase in the curvature of the CNRM shear-rotated hodograph within the lowest 1.5 km. Hence, both models show consistent small increases in both deeper-layer SRH but differ for future changes in SRH within the lowest 1 km. This outcome again reflects significant uncertainty in the representation of the detailed structure of the near-surface wind shear.

Overall, for the kinematic fields, the two models behave quite similarly to one another in both their representation of the historical climate (and hence their biases too) and in their projected changes in these fields with future climate change, with the stark exception of shear within the lowest 1 km where the two models give divergent outcomes. Both models project minimal changes to the hodograph shape and the bulk shear and SRH above 2 km. CNRM shows enhanced hodograph curvature within the lowest 2 km that translates to enhanced shear and SRH particularly within the lowest 1 km, whereas MPI shows minimal change at all levels. Hence, this outcome is highly uncertain.

c. *Interannual variability*

Finally, we briefly examine the representation of interannual variability in the annual-mean vertical structure of SCS environments and its projected changes with warming. Figure 8 displays the full range of variability, defined here as maximum minus minimum, in the annual-mean vertical profiles of relative humidity, integrated bulk shear, and SRH (note: all datasets are the same period length of 35 years). We focus on the most basic of our quantities but omit temperature simply because its variability is already quite small for the full database (Fig. 3).

For the historical climate, ERA5 indicates that there exists a substantial range of interannual variability in all three quantities. For RH (Fig. 8a), the range of variability in ERA5 of 15%–20% through the troposphere is reasonably well captured by the models. CNRM is particularly close to ERA5 in the middle and upper free troposphere, while MPI exhibits larger variability in the 4–6-km layer. Future changes in the simulated interannual range for RH are relatively modest for CNRM, while for MPI, the future range reduces at midlevels to align closely with CNRM.

For integrated bulk shear, the range in ERA5 is 4–5 m s^{-1} above 1 km and a smaller range at low levels. Both models exhibit a similar qualitative structure as ERA5 but a smaller magnitude below 3 km that is consistent between the two models. Above 3 km, CNRM has a slightly larger range than ERA5, while MPI has a smaller range. Future changes in the range are small for MPI, whereas for CNRM, the range decreases for deeper layers. Similarly, ERA5 exhibits significant interannual variability in SRH (Fig. 8c) that is underestimated by both MPI and CNRM, with very similar results between the two models. Future changes in variability are again small for MPI, but there is an increase in variability for CNRM at all levels. These changes in variability parallel that of the mean discussed above, wherein the kinematic structure in MPI remains relatively constant, while there is a future increase in low-level shear in CNRM.

Overall, the vertical thermodynamic and kinematic structure of these SCS environments can vary substantially from year to year, presumably owing to larger-scale climate variability, but the processes that control this variability may not be adequately captured in climate models. The low bias in kinematic variability in climate models indicates that the models cannot properly capture variability in the low-level hodograph even on interannual time scales. This is perhaps not surprising, as the complex interactions of the low-level flow with land surfaces and terrain may be at least partially captured in ERA5, owing to its higher resolution and its data assimilation scheme, but is unlikely to be reproduced by lower-resolution climate models. Additionally, there may be biases in capturing the variability of the vertical structure of the mean-state (i.e., non-SCS environment) flow field itself. Because the two models differ substantially in their representation of projected future changes to the kinematic profile, there is significant uncertainty in how its interannual variability may change with warming. What drives differences in the representation of interannual variability of the low-level wind field in climate models is beyond the scope of this study but is a worthy topic for future research.

d. *Implications*

Given recent work finding that tornadogenesis depends most strongly on shear in the lowest 1 km and possibly even lowest 0.5 km (Coffer et al. 2019, 2020), the increase in low-level shear suggests that the SRH ingredient for tornadogenesis could be enhanced when supercells form from a fixed bulk environment. However, the reduced boundary layer RH also increases the LCL, which is known to have a negative relationship with tornadogenesis (Thompson et al. 2004). Moreover, other less well-understood factors that influence tornadoes (e.g., updraft width) may change with warming as well that could potentially offset the changes in the shear structure analyzed here. Moreover, the poor representation of low-level shear in the historical climate as compared to ERA5, coupled with the lack of clear agreement in the structure of its projected change between our two models, indicates that this conclusion must be made with substantial caveat.

Meanwhile, an increase in MSE deficit found in CNRM would suggest the possibility of enhanced entrainment dilution. An increase in entrainment dilution may result in a reduction in

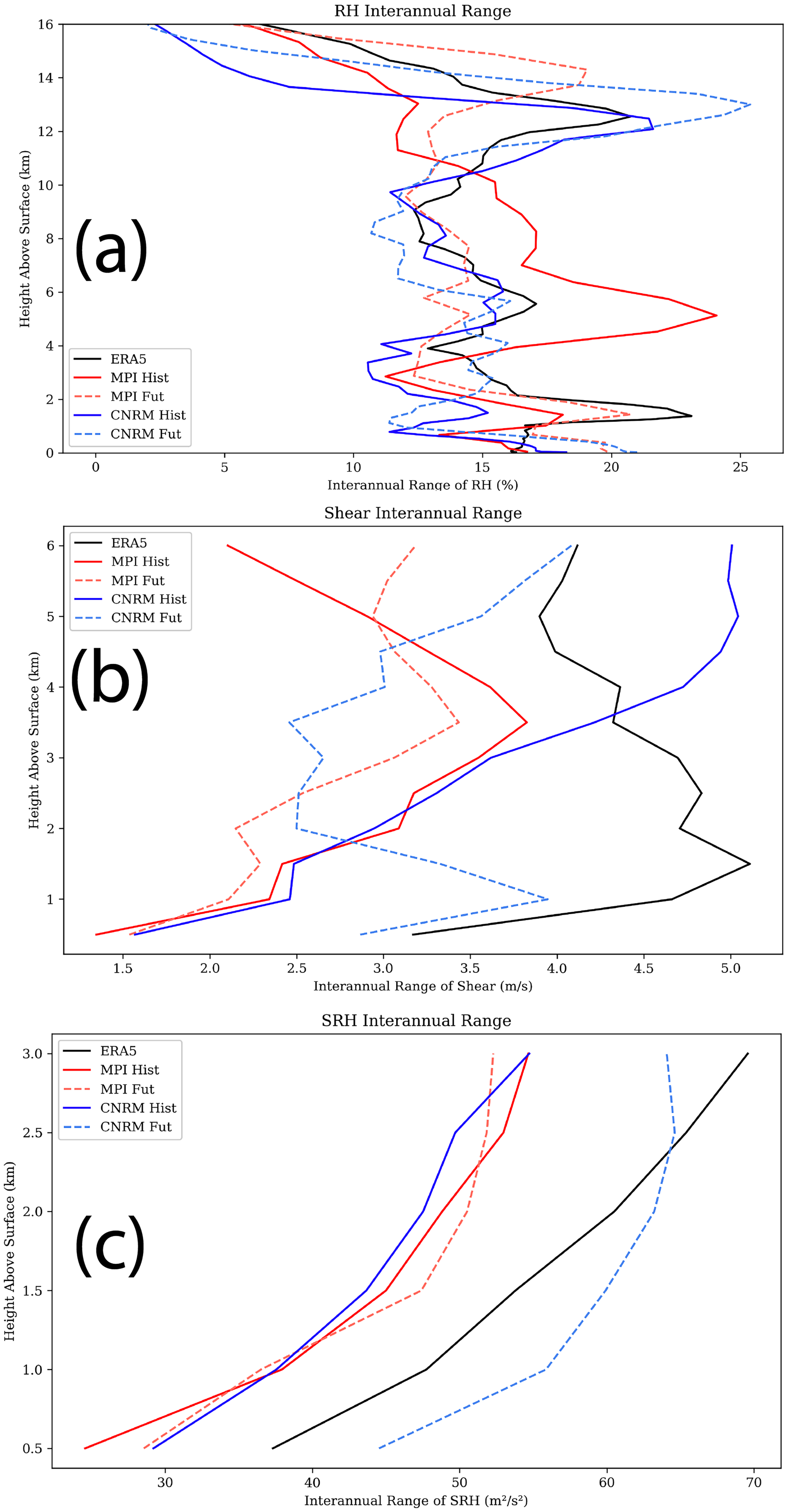

FIG. 8. Full range of variability in annual-mean vertical profiles from SCS environments across ERA5 and the historical and future simulations from both models for (a) RH, (b) integrated bulk shear, and (c) SRH.

the frequency of severe convective storms by reducing the true parcel CAPE from its undiluted value (Peters et al. 2020b, 2023a). The above interpretation is consistent with recent high-resolution regional modeling studies that find an increase in the frequency of SCS environments yet a decrease in the frequency of SCS activity over the central Great Plains region studied here (Ashley et al. 2023). This finding is typically ascribed to increases in convective inhibition, although changes in entrainment may play a similar role and are worthy of deeper study. Additionally, the slight decrease in the boundary layer relative humidity may increase LCLs, which may exacerbate these entrainment effects.

Overall, the vertical structure of these SCS soundings remains relatively constant with warming. Evaluation of the net effect of the modest changes to the vertical structure described above on severe thunderstorms and tornadoes themselves is too complex to be ascertained here, particularly given the deeper uncertainty associated with the most notable change (low-level shear).

4. Conclusions

Recent evidence suggests that severe thunderstorms and possibly tornadoes may become more frequent and/or intense in the future. Our understanding of this behavior is typically explained via changes in common vertically integrated (i.e., “bulk”) variables, such as CAPE and 0–6-km shear. However, the vertical structure of thermodynamic and kinematic profiles in severe convective storm environments possess many more degrees of freedom that can change independently of these standard bulk parameters. This work examined how climate change may affect the complete vertical structure of these environments for a fixed range of values of CAPE and S06, using soundings over the central Great Plains from two high-performing climate models for the high-end forcing ssp370 scenario. Hence, our results may be thought of as probing future climate changes in severe convective storm environments not associated with changes in CAPE and S06.

We summarize our primary results as follows:

1) Changes in the thermodynamic structure: temperature profiles warm relatively uniformly, with free-tropospheric lapse rates decreasing slightly. Relative humidity remains relatively constant, with the boundary layer becoming slightly drier (−2% to −6%) while the free troposphere becoming slightly moister (+2%). Free-tropospheric moist static energy deficit slightly increases aloft, with a deeper-layer increase in CNRM, consistent with the finding that MSE itself increases relatively uniformly with height with a slightly larger increase within the boundary layer.
2) Changes in the kinematic structure: Hodographs become more strongly curved in CNRM, due to slightly stronger southerly/southeasterly flow between 500 m and 1.5 km relative to flow near the surface, while the shear profile above 3 km remains largely unchanged. This behavior results in stronger wind shear within the lowest 1.5 km and greater storm-relative helicity within the lowest 1.5 km (which enhances SRH through all layers up to 3 km). However, there is little change in the hodograph in MPI at any level.
3) Overall, to first order, the vertical structure of SCS soundings warms approximately uniformly with height at constant relative humidity and the shear profile remains constant. There is a slight drying of the boundary layer and slight moistening of the free troposphere, and there is a slight increase in the MSE deficit aloft. CNRM shows an increase in low-level shear and 0–1-km SRH, but this change is not found in MPI, indicating that climate model projections for subtle changes in the low-level flow structure may be especially uncertain. Evaluation of the net response of these changes on severe thunderstorms and tornadoes themselves is too complex to be ascertained here.
4) There is substantial interannual variability in the vertical structure of relative humidity, bulk shear, and SRH within SCS environments. The kinematic variability particularly at low levels is strongly underestimated in the models, indicating significant uncertainty in the model representation of variability in the low-level wind field.

The findings of a slight reduction in the free-tropospheric lapse rate and boundary layer relative humidity with warming within our fixed ranges of CAPE and S06 are consistent with similar findings in Wang and Moyer (2023) for the entire distribution over summertime North America. We reiterate that such changes would be on top of changes associated with the expected large increases in CAPE with warming that would likely increase the intensity, and possibly frequency, of severe convective storms as noted in past studies. The relatively modest changes in the vertical structure found here suggest that changes in CAPE itself will still likely be the most important change in future SCS environments.

Our effort is a starting point for considering the full vertical structure of the thermodynamic and kinematic environment from climate models to better understand how severe thunderstorms and tornadoes may change with climate change. There remain multiple avenues for future work. Analysis of changes in the vertical structure could be extended to other geographic regions, particularly the Southeast United States, where the nature of severe thunderstorm environments and events are known to differ in complex ways from the Great Plains (Sherburn et al. 2016). This carries added importance given the recent shift in tornado activity toward the Southeast United States (Gensini and Brooks 2018). The use of clustering methods could help deal with the complexity of soundings taken from a wide array of environments (Hua and Anderson-Frey 2022). Moreover, recently developed theory for entraining CAPE (Peters et al. 2023a), which explicitly accounts for the role of entrainment of environmental air in the calculation of ascending parcel buoyancy, could be used to more directly quantify the effect of changes in entrainment on severe thunderstorm potential. Future work could test outcomes in limited-area numerical model experiments of individual storms. The outcomes can be compared against regional model experiments that can properly represent convective initiation and the array of convective forcing agents found in the real world. Additionally, future work may want to consider the components of storm-relative helicity, particularly environmental horizontal vorticity and storm-relative flow, given emerging research that it is specifically these two components of SRH that are associated with intense low-level mesocyclogenesis (Goldacker and Parker 2023).

Finally, we note that here we do not offer explanations for why key aspects of the vertical structure, such as the curvature of the low-level hodograph or the free-tropospheric relative humidity, do or do not change in the future. This type of understanding requires a broader analysis of how the synoptic-scale and large-scale circulation patterns (e.g., upper-level trough) will change and how this interacts with the land surface over the continental interior (e.g., Li et al. 2024). Such endeavors are highly complex but also worthwhile, especially for understanding climate change impacts on severe thunderstorm hazards given the critical importance of the near-surface wind structure for these phenomena.

Acknowledgments. The authors thank three anonymous reviewers for thorough and highly constructive feedback that greatly improved this manuscript. The authors were supported by the National Science Foundation (NSF) AGS Grants 1648681 and 2209052 and NASA FINESST Grant 19-EARTH20-0216. We also acknowledge the open-source Python community and particularly the authors and contributors to the Matplotlib (Hunter 2007), NumPy (Oliphant 2006), and MetPy (May et al. 2022) packages that were used to generate many of the analyses and figures.

Data availability statement. Six-hourly ERA5 reanalysis data were accessed on model levels from https://doi.org/10.5065/XV5R-5344 and for the near-surface and on pressure levels from https://doi.org/10.5065/BH6N-5N20 (European Centre for Medium-Range Weather Forecasts 2019). Six-hourly CMIP6 model historical and future experiment (ssp370, ssp585) data were accessed from https://esgf-node.llnl.gov/search/cmip6. Analyses were performed on the NCAR Cheyenne and Casper supercomputers (Computational and Information Systems Laboratory 2019) as well as on computational resources provided by Purdue Rosen Center for Advanced Computing (RCAC; McCartney et al. 2014). All data and code necessary to recreate each figure in the paper are available at https://zenodo.org/records/12802886.

REFERENCES

Agard, V., and K. Emanuel, 2017: Clausius–Clapeyron scaling of peak CAPE in continental convective storm environments. *J. Atmos. Sci.*, **74**, 3043–3054, https://doi.org/10.1175/JAS-D-16-0352.1.

Allen, J. T., D. J. Karoly, and G. A. Mills, 2011: A severe thunderstorm climatology for Australia and associated thunderstorm environments. *Aust. Meteor. Oceanogr. J.*, **61**, 143–158, https://doi.org/10.22499/2.6103.001.

Ashley, W. S., 2007: Spatial and temporal analysis of tornado fatalities in the United States: 1880–2005. *Wea. Forecasting*, **22**, 1214–1228, https://doi.org/10.1175/2007WAF2007004.1.

——, A. M. Haberlie, and V. A. Gensini, 2023: The future of supercells in the United States. *Bull. Amer. Meteor. Soc.*, **104**, E1–E21, https://doi.org/10.1175/BAMS-D-22-0027.1.

Betts, A. K., 1974: Further comments on "a comparison of the equivalent potential temperature and the static energy". *J. Atmos. Sci.*, **31**, 1713–1715, https://doi.org/10.1175/1520-0469(1974)031<1713:FCOCOT>2.0.CO;2.

——, 1975: Parametric interpretation of trade-wind cumulus budget studies. *J. Atmos. Sci.*, **32**, 1934–1945, https://doi.org/10.1175/1520-0469(1975)032<1934:PIOTWC>2.0.CO;2.

Brooks, H. E., J. W. Lee, and J. P. Craven, 2003: The spatial distribution of severe thunderstorm and tornado environments from global reanalysis data. *Atmos. Res.*, **67–68**, 73–94, https://doi.org/10.1016/S0169-8095(03)00045-0.

Brown, M., and C. J. Nowotarski, 2019: The influence of lifting condensation level on low-level outflow and rotation in simulated supercell thunderstorms. *J. Atmos. Sci.*, **76**, 1349–1372, https://doi.org/10.1175/JAS-D-18-0216.1.

Carlson, T., and F. Ludlam, 1968: Conditions for the occurrence of severe local storms. *Tellus*, **20**, 203–226, https://doi.org/10.3402/tellusa.v20i2.10002.

Chavas, D. R., and D. T. Dawson II, 2021: An idealized physical model for the severe convective storm environmental sounding. *J. Atmos. Sci.*, **78**, 653–670, https://doi.org/10.1175/JAS-D-20-0120.1.

——, and F. Li, 2022: Biases in CMIP6 historical U.S. severe convective storm environments driven by biases in mean-state near-surface moist static energy. *Geophys. Res. Lett.*, **49**, e2022GL098527, https://doi.org/10.1029/2022GL098527.

——, and J. Peters, 2023: Static energy deserves greater emphasis in the meteorology community. *Bull. Amer. Meteor. Soc.*, **104**, E1918–E1927, https://doi.org/10.1175/BAMS-D-22-0013.1.

Chen, J., A. Dai, Y. Zhang, and K. L. Rasmussen, 2020: Changes in convective available potential energy and convective inhibition under global warming. *J. Climate*, **33**, 2025–2050, https://doi.org/10.1175/JCLI-D-19-0461.1.

Christopoulos, C., and T. Schneider, 2021: Assessing biases and climate implications of the diurnal precipitation cycle in climate models. *Geophys. Res. Lett.*, **48**, e2021GL093017, https://doi.org/10.1029/2021GL093017.

Coffer, B. E., M. D. Parker, R. L. Thompson, B. T. Smith, and R. E. Jewell, 2019: Using near-ground storm relative helicity in supercell tornado forecasting. *Wea. Forecasting*, **34**, 1417–1435, https://doi.org/10.1175/WAF-D-19-0115.1.

——, M. Taszarek, and M. D. Parker, 2020: Near-ground wind profiles of tornadic and nontornadic environments in the United States and Europe from ERA5 reanalyses. *Wea. Forecasting*, **35**, 2621–2638, https://doi.org/10.1175/WAF-D-20-0153.1.

Computational and Information Systems Laboratory, 2019: Cheyenne: HPE/SGI ICE XA System (University Community Computing). National Center for Atmospheric Research, accessed 15 April 2020, https://doi.org/10.5065/D6RX99HX.

Diffenbaugh, N. S., M. Scherer, and R. J. Trapp, 2013: Robust increases in severe thunderstorm environments in response to greenhouse forcing. *Proc. Natl. Acad. Sci. USA*, **110**, 16 361–16 366, https://doi.org/10.1073/pnas.1307758110.

Doswell, C. A., 2001: Severe convective storms—An overview. *Severe Convective Storms*, Springer, 1–26.

Douville, H., S. Qasmi, A. Ribes, and O. Bock, 2022: Global warming at near-constant tropospheric relative humidity is supported by observations. *Commun. Earth Environ.*, **3**, 237, https://doi.org/10.1038/s43247-022-00561-z.

European Centre for Medium-Range Weather Forecasts, 2019: ERA5 reanalysis (0.25 Degree Latitude-Longitude Grid).

Research Data Archive at the National Center for Atmospheric Research, Computational and Information Systems Laboratory, accessed 15 April 2020, https://doi.org/10.5065/BH6N-5N20.

Eyring, V., S. Bony, G. A. Meehl, C. A. Senior, B. Stevens, R. J. Stouffer, and K. E. Taylor, 2016: Overview of the Coupled Model Intercomparison Project Phase 6 (CMIP6) experimental design and organization. *Geosci. Model Dev.*, **9**, 1937–1958, https://doi.org/10.5194/gmd-9-1937-2016.

Gensini, V. A., 2021: Severe convective storms in a changing climate. *Climate Change and Extreme Events*, Elsevier, 39–56.

——, and T. L. Mote, 2015: Downscaled estimates of late 21st century severe weather from CCSM3. *Climatic Change*, **129**, 307–321, https://doi.org/10.1007/s10584-014-1320-z.

——, and H. E. Brooks, 2018: Spatial trends in United States tornado frequency. *npj Climate Atmos. Sci.*, **1**, 38, https://doi.org/10.1038/s41612-018-0048-2.

Goldacker, N. A., and M. D. Parker, 2023: Assessing the comparative effects of storm-relative helicity components within right-moving supercell environments. *J. Atmos. Sci.*, **80**, 2805–2822, https://doi.org/10.1175/JAS-D-22-0253.1.

Guarriello, F., C. J. Nowotarski, and C. C. Epifanio, 2018: Effects of the low-level wind profile on outflow position and near-surface vertical vorticity in simulated supercell thunderstorms. *J. Atmos. Sci.*, **75**, 731–753, https://doi.org/10.1175/JAS-D-17-0174.1.

Hersbach, H., and Coauthors, 2020: The ERA5 global reanalysis. *Quart. J. Roy. Meteor. Soc.*, **146**, 1999–2049, https://doi.org/10.1002/qj.3803.

Hoogewind, K. A., M. E. Baldwin, and R. J. Trapp, 2017: The impact of climate change on hazardous convective weather in the United States: Insight from high-resolution dynamical downscaling. *J. Climate*, **30**, 10 081–10 100, https://doi.org/10.1175/JCLI-D-16-0885.1.

Hu, J., A. Bailey, J. Nusbaumer, S. Dee, C. Sasser, and J. Worden, 2022: Tracking shallow convective mixing and its influence on low-level clouds with stable water isotopes in vapor. *J. Geophys. Res. Atmos.*, **127**, e2021JD035355, https://doi.org/10.1029/2021JD035355.

Hua, Z., and A. K. Anderson-Frey, 2022: Self-organizing maps for the classification of spatial and temporal variability of tornado-favorable parameters. *Mon. Wea. Rev.*, **150**, 393–407, https://doi.org/10.1175/MWR-D-21-0168.1.

Hunter, J. D., 2007: Matplotlib: A 2D graphics environment. *Comput. Sci. Eng.*, **9**, 90–95, https://doi.org/10.1109/MCSE.2007.55.

Jo, E., and S. Lasher-Trapp, 2022: Entrainment in a simulated supercell thunderstorm. Part II: The influence of vertical wind shear and general effects upon precipitation. *J. Atmos. Sci.*, **79**, 1429–1443, https://doi.org/10.1175/JAS-D-21-0289.1.

Lasher-Trapp, S., E. Jo, L. R. Allen, B. N. Engelsen, and R. J. Trapp, 2021: Entrainment in a simulated supercell thunderstorm. Part I: The evolution of different entrainment mechanisms and their dilutive effects. *J. Atmos. Sci.*, **78**, 2725–2740, https://doi.org/10.1175/JAS-D-20-0223.1.

Lepore, C., R. Abernathey, N. Henderson, J. T. Allen, and M. K. Tippett, 2021: Future global convective environments in CMIP6 models. *Earth's Future*, **9**, e2021EF002277, https://doi.org/10.1029/2021EF002277.

——, J. Allen, and R. Abernathey, 2022: xcape (v0.1.4). Zenodo, accessed 10 January 2022, https://doi.org/10.5281/zenodo.5270332.

Li, F., D. R. Chavas, K. A. Reed, and D. T. Dawson II, 2020: Climatology of severe local storm environments and synoptic-scale features over North America in ERA5 reanalysis and CAM6 simulation. *J. Climate*, **33**, 8339–8365, https://doi.org/10.1175/JCLI-D-19-0986.1.

——, ——, ——, N. Rosenbloom, and D. T. Dawson II, 2021: The role of elevated terrain and the Gulf of Mexico in the production of severe local storm environments over North America. *J. Climate*, **34**, 7799–7819, https://doi.org/10.1175/JCLI-D-20-0607.1.

——, ——, B. Medeiros, K. A. Reed, and K. Rasmussen, 2024: Upstream surface roughness and terrain are strong drivers of the contrast in tornado potential between North and South America. *Proc. Natl. Acad. Sci. USA*, **121**, e2315425121, https://doi.org/10.1073/pnas.2315425121.

May, R. M., and Coauthors, 2022: MetPy: A meteorological Python library for data analysis and visualization. *Bull. Amer. Meteor. Soc.*, **103**, E2273–E2284, https://doi.org/10.1175/BAMS-D-21-0125.1.

McCartney, G., T. Hacker, and B. Yang, 2014: Empowering faculty: A campus cyberinfrastructure strategy for research communities. Educause Review, accessed 14 July 2014, https://er.educause.edu/articles/2014/7/empowering-faculty-a-campus-cyberinfrastructure-strategy-for-research-communities.

McCaul, E. W., Jr., and M. L. Weisman, 2001: The sensitivity of simulated supercell structure and intensity to variations in the shapes of environmental buoyancy and shear profiles. *Mon. Wea. Rev.*, **129**, 664–687, https://doi.org/10.1175/1520-0493(2001)129<0664:TSOSSS>2.0.CO;2.

McCaul, E. W., and C. Cohen, 2002: The impact on simulated storm structure and intensity of variations in the mixed layer and moist layer depths. *Mon. Wea. Rev.*, **130**, 1722–1748, https://doi.org/10.1175/1520-0493(2002)130<1722:TIOSSS>2.0.CO;2.

Nixon, C. J., and J. T. Allen, 2022: Distinguishing between hodographs of severe hail and tornadoes. *Wea. Forecasting*, **37**, 1761–1782, https://doi.org/10.1175/WAF-D-21-0136.1.

Oliphant, T. E., 2006: *A Guide to NumPy*. Vol. 1. Trelgol Publishing, 261 pp.

O'Neill, M. E., L. Orf, G. M. Heymsfield, and K. Halbert, 2021: Hydraulic jump dynamics above supercell thunderstorms. *Science*, **373**, 1248–1251, https://doi.org/10.1126/science.abh3857.

Peters, J. M., H. Morrison, C. J. Nowotarski, J. P. Mulholland, and R. L. Thompson, 2020a: A formula for the maximum vertical velocity in supercell updrafts. *J. Atmos. Sci.*, **77**, 3747–3757, https://doi.org/10.1175/JAS-D-20-0103.1.

——, C. J. Nowotarski, J. P. Mulholland, and R. L. Thompson, 2020b: The influences of effective inflow layer streamwise vorticity and storm-relative flow on supercell updraft properties. *J. Atmos. Sci.*, **77**, 3033–3057, https://doi.org/10.1175/JAS-D-19-0355.1.

——, J. P. Mulholland, and D. R. Chavas, 2022: Generalized lapse rate formulas for use in entraining CAPE calculations. *J. Atmos. Sci.*, **79**, 815–836, https://doi.org/10.1175/JAS-D-21-0118.1.

——, D. R. Chavas, C.-Y. Su, H. Morrison, and B. E. Coffer, 2023a: An analytic formula for entraining CAPE in midlatitude storm environments. *J. Atmos. Sci.*, **80**, 2165–2186, https://doi.org/10.1175/JAS-D-23-0003.1.

——, B. E. Coffer, M. D. Parker, C. J. Nowotarski, J. P. Mulholland, C. J. Nixon, and J. T. Allen, 2023b: Disentangling the influences of storm-relative flow and horizontal streamwise vorticity on low-level mesocyclones in supercells. *J. Atmos. Sci.*, **80**, 129–149, https://doi.org/10.1175/JAS-D-22-0114.1.

Pielke, R., Jr., M. G. Burgess, and J. Ritchie, 2022: Plausible 2005–2050 emissions scenarios project between 2°C and 3°C of warming by 2100. *Environ. Res. Lett.*, **17**, 024027, https://doi.org/10.1088/1748-9326/ac4ebf.

Santer, B. D., and Coauthors, 2013: Human and natural influences on the changing thermal structure of the atmosphere. *Proc. Natl. Acad. Sci. USA*, **110**, 17 235–17 240, https://doi.org/10.1073/pnas.1305332110.

Seeley, J. T., and D. M. Romps, 2015: The effect of global warming on severe thunderstorms in the United States. *J. Climate*, **28**, 2443–2458, https://doi.org/10.1175/JCLI-D-14-00382.1.

——, N. Jeevanjee, and D. M. Romps, 2019: FAT or FITT: Are anvil clouds or the tropopause temperature invariant? *Geophys. Res. Lett.*, **46**, 1842–1850, https://doi.org/10.1029/2018GL080096.

Sherburn, K. D., M. D. Parker, J. R. King, and G. M. Lackmann, 2016: Composite environments of severe and nonsevere high-shear, low-CAPE convective events. *Wea. Forecasting*, **31**, 1899–1927, https://doi.org/10.1175/WAF-D-16-0086.1.

Singh, M. S., and P. A. O'Gorman, 2012: Upward shift of the atmospheric general circulation under global warming: Theory and simulations. *J. Climate*, **25**, 8259–8276, https://doi.org/10.1175/JCLI-D-11-00699.1.

Strader, S. M., and W. S. Ashley, 2015: The expanding bull's-eye effect. *Weatherwise*, **68**, 23–29, https://doi.org/10.1080/00431672.2015.1067108.

Taszarek, M., J. T. Allen, P. Groenemeijer, R. Edwards, H. E. Brooks, V. Chmielewski, and S.-E. Enno, 2020a: Severe convective storms across Europe and the United States. Part I: Climatology of lightning, large hail, severe wind, and tornadoes. *J. Climate*, **33**, 10 239–10 261, https://doi.org/10.1175/JCLI-D-20-0345.1.

——, ——, T. Púčik, K. A. Hoogewind, and H. E. Brooks, 2020b: Severe convective storms across Europe and the United States. Part II: ERA5 environments associated with lightning, large hail, severe wind, and tornadoes. *J. Climate*, **33**, 10 263–10 286, https://doi.org/10.1175/JCLI-D-20-0346.1.

——, ——, H. E. Brooks, N. Pilguj, and B. Czernecki, 2021: Differing trends in United States and European severe thunderstorm environments in a warming climate. *Bull. Amer. Meteor. Soc.*, **102**, E296–E322, https://doi.org/10.1175/BAMS-D-20-0004.1.

Thompson, D. W., P. Ceppi, and Y. Li, 2019: A robust constraint on the temperature and height of the extratropical tropopause. *J. Climate*, **32**, 273–287, https://doi.org/10.1175/JCLI-D-18-0339.1.

Thompson, R. L., R. Edwards, and C. M. Mead, 2004: An update to the supercell composite and significant tornado parameters. Preprints, *22nd Conf. on Severe Local Storms*, Hyannis, MA, Amer. Meteor. Soc. P.81, https://www.spc.noaa.gov/publications/thompson/stp_scp.pdf.

Tippett, M. K., J. T. Allen, V. A. Gensini, and H. E. Brooks, 2015: Climate and hazardous convective weather. *Curr. Climate Change Rep.*, **1**, 60–73, https://doi.org/10.1007/s40641-015-0006-6.

Trapp, R. J., K. A. Hoogewind, and S. Lasher-Trapp, 2019: Future changes in hail occurrence in the United States determined through convection-permitting dynamical downscaling. *J. Climate*, **32**, 5493–5509, https://doi.org/10.1175/JCLI-D-18-0740.1.

Wang, Z., and E. J. Moyer, 2023: Robust relationship between midlatitudes CAPE and moist static energy surplus in present and future simulations. *Geophys. Res. Lett.*, **50**, e2023GL104163, https://doi.org/10.1029/2023GL104163.

WMO/OMM/BMO, 1992: International meteorological vocabulary. Secretariat of the World Meteorological Organization Tech. Rep. 182, 782 pp.

Zhang, G. J., 2009: Effects of entrainment on convective available potential energy and closure assumptions in convective parameterization. *J. Geophys. Res.*, **114**, D07109, https://doi.org/10.1029/2008JD010976.

Zhang, Q., B. Liu, S. Li, and T. Zhou, 2023: Understanding models' global sea surface temperature bias in mean state: From CMIP5 to CMIP6. *Geophys. Res. Lett.*, **50**, e2022GL100888, https://doi.org/10.1029/2022GL100888.